Robust and Fast Sliding-Mode Control for a DC-DC Current-Source Parallel-Resonant Converter

Mohammad Moradi Ghahderijani [1*], Miguel Castilla [1], Arash Momeneh [2], Jaume Miret [1], Luis García de Vicuña [1]

[1] Department of Electronic Engineering, Technical University of Catalonia, Avda. Victor Balaguer s/n 08800 Vilanova i la Geltrú, Spain
[2] Department of Powertrain, Applus IDIADA Group, 43710 Santa Oliva, Tarragona, Spain
[*] mohammad.moradi.ghahderijani@upc.edu

Abstract: Modern DC-DC resonant converters are normally build around a voltage-source series-resonant converter. This study aims to facilitate the practical use of current-source parallel-resonant converters due to their outstanding properties. To this end, the study presents a sliding-mode control scheme, which provides the following features to the closed-loop system: 1) high robustness to external disturbances and parameter variations and 2) fast transient response during large and abrupt load changes. In addition, a design procedure for determining the values of the control parameters is presented. The theoretical contributions of the paper are experimentally validated by selected tests on a laboratory prototype.

1. Introduction

Resonant converters play a significant role in today's energy conversion systems due to its reduced electromagnetic interference, lower switching losses, and higher efficiency [1]-[3]. DC-DC energy conversion is a fascinating application of great importance for these converters [4]-[6]. Robotics, battery charging, electrostatic precipitators, X-ray power supply, and distributed power systems are just a few examples in which DC-DC resonant converters are used today [7]-[13].

The typical resonant converter used in DC-DC applications is a voltage-source topology with series resonant tank [14]-[16]. The current-source parallel-resonant converter (CSPRC) is an alternative solution for such application. The features of this topology were extensively studied in [17]-[21]. Compared to the series resonant converter, the CSPRC offers well-known advantages such as non-pulsating input current, low stress for switches, simple driving circuitry, short circuit protection capabilities, and simple paralleling properties. However, it is a more complex system, which has possibly slowed down its use on practical applications. In fact, through a literature review, it is clearly observed that the series resonant converter is mostly used in comparison with the CSPRC converter.

Nowadays, new applications of resonant converters growth, such as for example in contactless energy transfer systems. For this application, a modulation scheme for a CSPRC system was presented in [20], [21]. These works revealed the facility of the CSPRC to absorb the typical inductance variation of the resonant tank in order to force the converter to work at the resonant frequency. However, in this works, the converter operates in open loop. Thus, an operation with low robustness against external disturbances and parameter variations is expected. The identification of this weaknesses is actually the starting point of this paper. The main objective of the paper is to design a robust and fast closed-loop control scheme for the CSPRC to be used in DC-DC conversion applications.

Sliding mode control is one of the major operation modes of variable structure control as a form of discontinuous nonlinear control systems [22]. Sliding-mode control offers the desired static and dynamic characteristics (i.e., robust operation and fast transient response). In [23], a sliding-mode control for the CSPRC was presented. However, some critical issues were not conveniently addressed in the proposal: 1) the control configuration was not designed for applications which are subjected to significant disturbances, so that the control scheme must be revised and updated for this new scenario, 2) the modulator exhibits high sensitivity to parameter variations, and 3) the transient response is not good enough, especially during large and abrupt load changes. In addition, the theoretical predictions in [23] were not validated experimentally, which is really essential for practical applications.

In this paper, an updated version of the sliding-mode control presented in [23] is introduced. The superior properties of the closed-loop controlled system are: 1) high robustness to external disturbances and parameter variations and 2) fast transient response during large load changes. To this end, a novel modulator and two control loops with improved configuration are developed and designed for the CSPRC.

The paper is structured as follows. In Section 2, a general description of the CSPRC is presented. Dynamic modelling of the converter is introduced in Section 3. Section 4 presents the novel sliding-mode control for this converter. Section 5 introduces the design procedure of the proposed control system. Section 6 validates the theoretical contributions by selected simulation and experimental results. Finally, Section 7 gives the summary and presents the open research topics in this field.

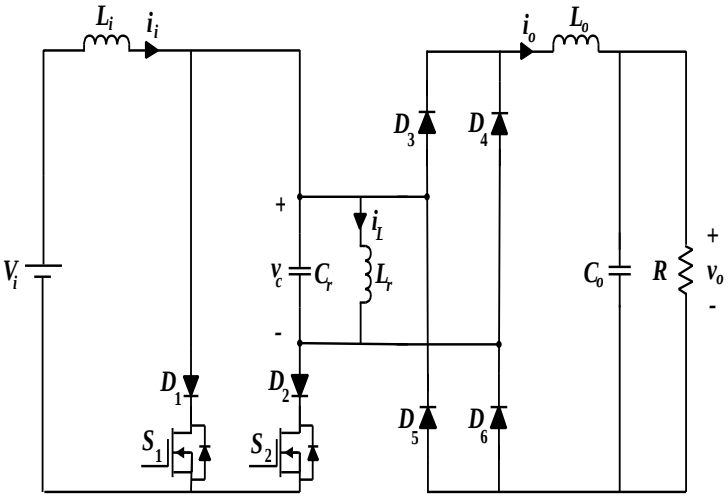

Fig. 1. *Power circuit of the class-D CSPRC*

2. System description

The power circuit of a typical Class-D CSPRC is shown in Fig. 1. This converter is composed of an input large choke inductor L_i, and a second-order parallel-resonant circuit (L_r and C_r). The resonant tank is driven by a class-D inverter in order to obtain high-frequency resonant waveforms. These waveforms are then converted back to DC level through a passive full-bridge diode rectifier, loaded with a second-order low-pass filter (L_o and C_o). The load is modelled as the resistor R.

Fig. 2 and 3 show the operation principle of the converter in two different modes of energising and de-energising modes. In energising mode, when the switch S1 is OFF and S2 is ON, input current flows through the LC resonant tank. Therefore, energy will be transferred from DC input source to the resonant tank. In de-energising mode, when S1 is ON and S2 is OFF, the input current passes through the left leg and the energy kept in the resonant tank is partially discharged to the load.

This principle of operation provides an amplitude-modulated sinusoidal voltage in the resonant capacitor. In addition, regarding the synchronization process explained in Section 4, the converter operates exactly at the resonant frequency defined as

$$f_o = \frac{1}{2\pi\sqrt{L_r\, C_r}} \tag{1}$$

Therefore, changes of the resonant component values will be detected by the control circuit, thus updating the operating frequency to the new value of f_o, as described in Section 4.

3. Dynamic modelling

3.1. State-Space Model

The state-state model of the amplitude-modulated converter shown in Fig. 1 can be written in a compact form by using the variable u (which denotes the operating mode of the converter). According to Fig. 2 and 3, the state-space model is expressed as:

$$\frac{di_i}{dt} = \frac{1}{L_i}\left[V_i - u\left(\frac{1+sgn(v_c)}{2}\right) v_c\right] \tag{2}$$

$$\frac{di_L}{dt} = \frac{1}{L_r}\, v_c \tag{3}$$

$$\frac{di_o}{dt} = \frac{1}{L_o}\left[|v_c| - v_o\right] \tag{4}$$

$$\frac{dv_c}{dt} = \frac{1}{C_r}\left[u\left(\frac{1+sgn(v_c)}{2}\right) i_i - i_L - i_o\, sgn(v_c)\right] \tag{5}$$

$$\frac{dv_o}{dt} = \frac{1}{C_o}\left[i_o - \frac{v_o}{R}\right] \tag{6}$$

where i_i is the input current variable, v_c and i_L are the resonant state variables, and v_o and i_o are the output filter state variables. In addition, u is the output signal of the control system which is a discrete-time variable. This signal determines the operational mode of energising or de-energising. Note that, for simplicity, to derive this model, all components are assumed ideal and no parasitic effects have been considered in this study. The error produced by this simplification is absorbed by the controller as proven by the experimental results presented in Section 6.

3.2. Averaged Large-Signal Model in Open Loop

For control design, an averaged model of the converter is used instead of the switching model in (2)-(6). In this case, the slow state-variables are i_i, i_o and v_o, while the resonant circuit state-variables (i_L and v_c) are considered as the fast variables.

Given that the resonant tank frequency is very large compared to the cut-off frequency of the output filter, there is a negligible ripple in the output filter state variables. Hence, these variables can be approximated accurately by means of their time-varying average values $\bar{i}_o$ and $\bar{v}_o$.

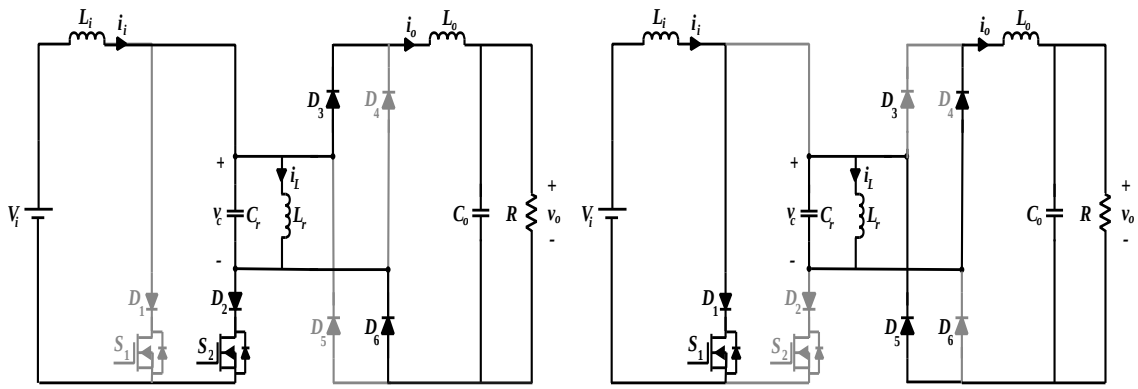

Fig. 2. *Operational modes of the converter in energising mode (u=1)*
a $v_c > 0$
b $v_c < 0$

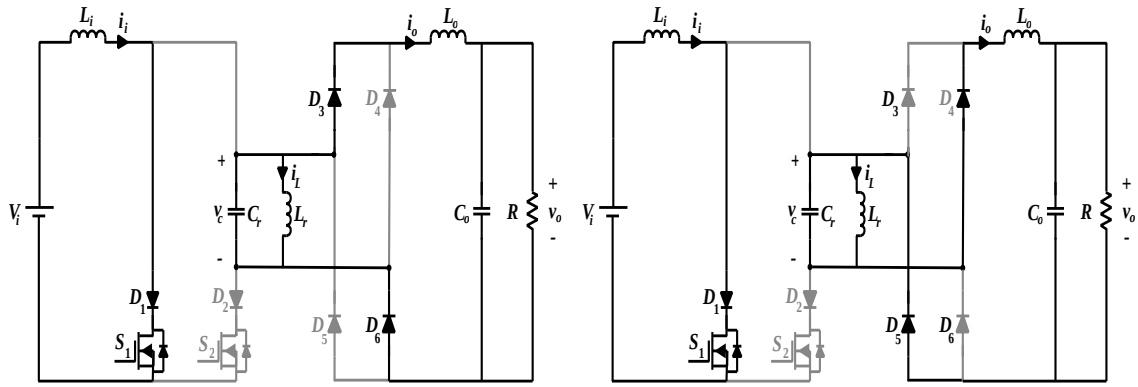

Fig. 3. *Operational modes of the converter in de-energising mode (u=0)*
a $v_c > 0$
b $v_c < 0$

Furthermore, the fast variables can be approximated by the following sinusoidal functions:

$$v_c = V_c \, sin(\omega_o t) \tag{7}$$

$$i_L = I_L \, sin(\omega_o t - \Phi) \tag{8}$$

Note that the amplitude modulation forces these state variables to work at exactly the resonant frequency ω_o and forces the phase angle related to the resonant current to be continually zero.

Replacing (7) and (8) into (2)-(6), and applying the methodology used in [23], the averaged model is obtained as shown in Fig. 4 and formulated in (9)-(12):

$$\frac{d\bar{i}_i}{dt} = \frac{1}{L_i}\left[V_i - \bar{u}\frac{\bar{v}_c}{2}\right] \tag{9}$$

$$\frac{d\bar{v}_c}{dt} = \frac{1}{C_{eq}}\left[\bar{u}\,\frac{\bar{i}_i}{2} - \bar{i}_o\right] \tag{10}$$

$$\frac{d\bar{i}_o}{dt} = \frac{1}{L_o}\,[\bar{v}_c - \bar{v}_o] \tag{11}$$

$$\frac{d\bar{v}_o}{dt} = \frac{1}{C_o}\left[\bar{i}_o - \frac{\bar{v}_o}{R}\right] \tag{12}$$

where $\bar{u}$ is the control input, the symbol − denotes averaged value over a half switching cycle, and the equivalent resonant capacitor is defined as:

$$C_{eq} = \frac{\pi^2}{4} C_r \tag{13}$$

From (9), the voltage gain of the converter can be derived assuming that the control input in steady-state is U ($0 < U < 1$):

$$\frac{V_o}{V_i} = \frac{2}{U} \tag{14}$$

Note that the converter has a step-up voltage behaviour with a double gain compared with the conventional boost converter.

3.3. Large-Signal Model Verification

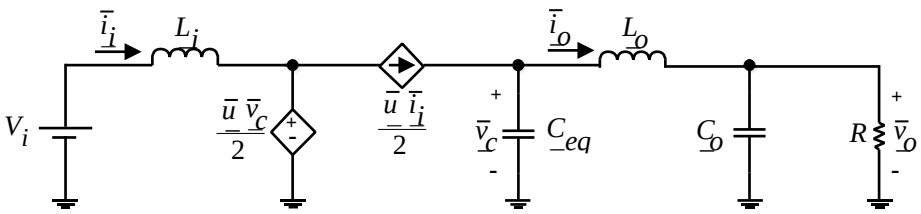

Fig. 4. *Averaged model of the class-D CSPRC with amplitude modulation.*

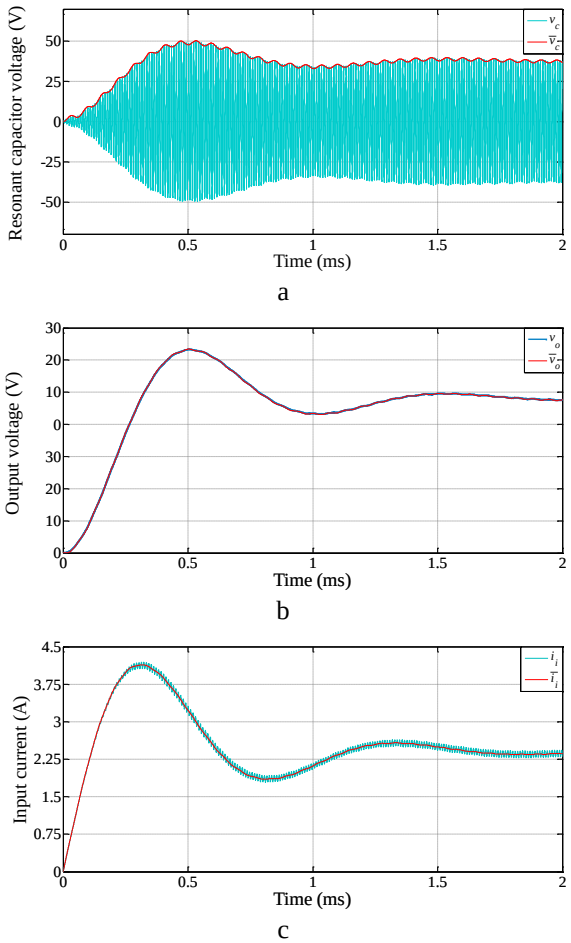

Fig. 5. *Comparison of waveforms generated by the state-space model and the averaged model.*
a Resonant capacitor voltage
b Output voltage
c Input current

The accuracy of this developed large-signal model is proven by simulation, taking into account the comparison with the state-space model presented in (2)-(6) as illustrated in Fig. 5. The power system parameters used in the simulation have been summarized in Table 1. The results show a good agreement between the models for both transient and steady states. Hence, the averaged large signal model can be used in control design process.

4. Proposed control scheme

This Section introduces the sliding mode controller for the parallel-resonant converter with amplitude modulation. This control configuration constitutes the first contribution of this paper. Furthermore, a comparison with the control scheme in [23] is also presented.

Table 1 Values of the power components

Symbol	Quantity	Value
V_i	Input voltage	12 V
L_i	Input filter inductor	300 μH
C_r	Resonant capacitor	470 nF
L_r	Nominal resonant inductor	5.3 μH
$L_{r,max}$	Maximum resonant inductor	13.3 μH
L_o	Output filter inductor	100 μH
C_o	Output filter capacitor	470 μF
R	Full-load resistor	20 Ω

4.1. Control Objectives

The proposed control scheme is responsible for satisfying the following control objectives. The first aim is voltage regulation. The output voltage in steady-state must be regulated to the reference voltage, even in presence of power component variations and load changes. The second control objective is to obtain high robustness against power component variations in order to operate continuously the converter exactly at resonant frequency. It is well-known that power devices suffer changes by aging, and temperature variations, so operating at resonant frequency requires an online adaptation to these changes. The third (and last) control objective is a fast transient response during large step changes in the load.

4.2. Control Configuration

This Section introduces a sliding-mode control configuration for the amplitude modulated class-D CSPRC system as shown in Fig. 6.

The averaged dynamic model of this converter coincides with the dynamic model of a conventional boost converter with a high-order output filter. Thus, a current mode control is a good option to control this converter. To this end, a current-mode sliding surface is implemented as:

$$S = i_{ref} - i_i \tag{15}$$

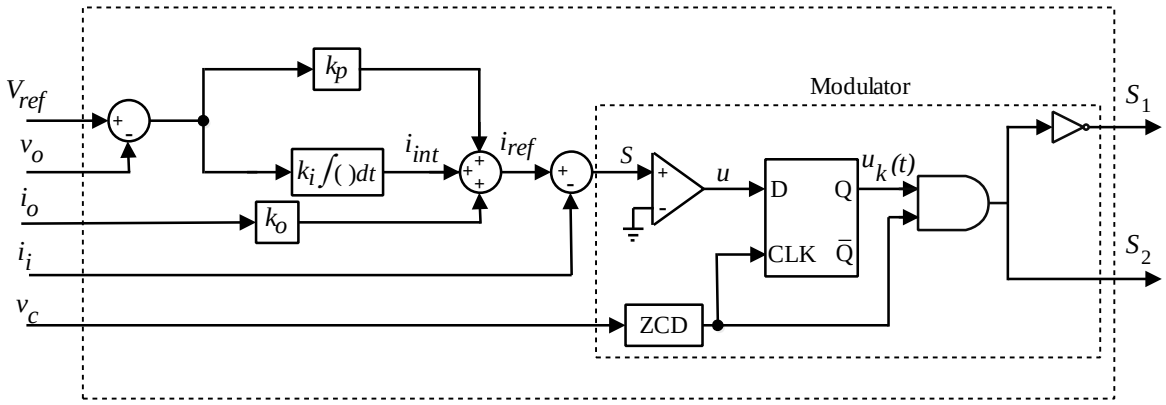

Fig. 6. *Block diagram of the proposed sliding-mode controller*

$$i_{ref} = k_p\left(V_{ref} - v_o\right) + i_{int} + k_o i_o \tag{16}$$

$$i_{int} = k_i\int\left(V_{ref} - v_o\right)dt \tag{17}$$

The control scheme is composed of an outer voltage and inner current loop as well as a robust amplitude modulator.

The outer loop is responsible for output voltage regulation, consisting of two control terms: a feedback term that tries to eliminate the output voltage error using a PI regulator and a feedforward term of the output current. The feedback term ensures that the output voltage matches the reference voltage in steady state, thus compensating the effects of un-modelled elements such as parasitic resistors. In the case of load-step changes, the feed-forward term helps the modulator to rapidly find an appropriate control signal to ensure a fixed-output voltage, yielding in a fast transient response. The gain value of the feed-forward term is defined as below:

$$k_o = \frac{V_{ref}}{V_i} \tag{18}$$

In the inner current loop, the input current will properly track the reference current as imposed by the proposed sliding surface. In addition, the control signal u is generated and synchronized to the resonant capacitor voltage by the modulator using a comparator, a D flip-flop and a zero crossing detection (ZCD). Note that the output signal of the ZCD block is used to first synchronize the control signal u, and then to generate the gating signals for the resonant converter switches i.e., S1 and S2. This modulator produces a robust operation against external disturbances and parameter variations as will be demonstrated later. The synchronized control signal is then applied to a logic circuit to provide the driving signals sent to the power switches.

4.3. Comparison with Conventional Scheme

As far as the authors know, [23] is the only reference studying a sliding-mode control scheme for the amplitude-modulated CSPRC. Thus, the control presented in [23] is used here as a reference to be compared with the proposed control.

In [23], the transient response is not fast enough and a relatively high voltage deviation is noticed during the load step change. In the proposed control scheme, an output current feed-forward term $k_o i_o$ is added, providing a fast transient response and a low voltage deviation against load step changes.

Furthermore, the amplitude modulation technique used in [23] is not robust against parameter variations. The reason is that the operation of the modulator is synchronized with a fixed clock, working in a pre-defined frequency. As a consequence, for instance, by changing the resonant inductor, the resonant frequency is changed. Therefore, the resonant converter works at a frequency different to the resonant frequency, yielding higher switching losses and lower efficiency. This drawback is effectively eliminated by introducing the adaptive modulator shown in Fig. 3, which provides a robust system against parameter variations to successfully track the resonant frequency in different conditions.

5. Control design

This section presents the control design procedure for the proposed sliding-mode control scheme. The closed-loop dynamics of the system is first obtained based on the equivalent control theory [24]. This model is then linearized around its equilibrium point to be used in the stability analysis. The design conditions for determining the control parameters constitute the second contribution of this paper.

5.1. Closed-Loop Large-Signal Model

To obtain the closed-loop dynamics of the system, the first step is to satisfy the ideal sliding properties (19) and (20). Such properties are considered to ensure the desired closed-loop dynamics [25].

$$S\left(i_i . v_o . i_o . i_{int}\right) = 0 \tag{19}$$

$$\frac{ds}{dt}\left(i_i . v_o . i_o . i_{int}\right) = 0 \tag{20}$$

Therefore, the equivalent control signal $\bar{u}_{eq}$ is obtained as:

$$\bar{u}_{eq} = \frac{2\,V_i}{\bar{v}_c} + \frac{2\,L_i}{\bar{v}_c}\left[k_i\left(\bar{v}_o - V_{ref}\right) - \frac{k_o(\bar{v}_c - \bar{v}_o)}{L_o} + \frac{k_p(\bar{i}_o - \bar{v}_o/R)}{C_o}\right] \tag{21}$$

By replacing $\bar{u}$ with $\bar{u}_{eq}$ in (9)-(10) and re-writing (17), the large-signal model is obtained as (22)-(24), as well as (11)-(12).

$$\frac{d\bar{i}_i}{dt} = \frac{1}{L_o C_o}\Big[-L_o C_o k_i(\bar{v}_o - V_{ref}) + C_o k_o(\bar{v}_c - \bar{v}_o) - L_o k_p(\bar{i}_o - \frac{\bar{v}_o}{R})\Big] \quad (22)$$

$$\frac{d\bar{v}_c}{dt} = \frac{1}{C_{eq}\bar{v}_c}\left(\left[L_i\bar{i}_i\left(k_i(\bar{v}_o - V_{ref}) - \frac{k_o(\bar{v}_c - \bar{v}_o)}{L_o} + \frac{k_p(\bar{i}_o - \bar{v}_o/R)}{C_o}\right) + \frac{V_i}{L_i}\right] - \bar{i}_o\bar{v}_c\right) \quad (23)$$

$$\frac{d\bar{i}_{int}}{dt} = k_i(V_{ref} - \bar{v}_o) \quad (24)$$

Note that the closed-loop dynamic model has order five, four equations for the resonant converter (11), (12), (22) and (23) and one equation for the control (24).

5.2. Closed-Loop Small-Signal Model

The stability analysis presented in next subsection is based on a linearized small-signal model. In this subsection, the closed-loop large-signal model is linearized.

In steady-state conditions, the averaged variables reach their equilibrium point. By considering $d\bar{i}_i/dt = 0$, $d\bar{v}_c/dt = 0$, $d\bar{i}_o/dt = 0$ and $d\bar{v}_o/dt = 0$, the equilibrium point of the closed-loop model (11), (12), (22), (23), and (24) can be expressed as:

$$V_o = V_{ref} \quad (25)$$

$$V_c = V_{ref} \quad (26)$$

$$I_o = \frac{V_{ref}}{R} \quad (27)$$

$$I_i = \frac{V_{ref}^2}{R\,V_i} \quad (28)$$

These equilibrium point values are then used to linearize the closed-loop large-signal model around this point. The small-signal model can be written as:

$$\frac{d}{dt}\begin{bmatrix}\hat{i}_i\\ \hat{v}_c\\ \hat{i}_o\\ \hat{v}_o\\ \hat{i}_{int}\end{bmatrix} = \begin{bmatrix}0 & J_{12} & J_{13} & J_{14} & 0\\ J_{21} & J_{22} & J_{23} & J_{24} & 0\\ 0 & 1/L_o & 0 & -1/L_o & 0\\ 0 & 0 & 1/C_o & -1/(R.C_o) & 0\\ 0 & 0 & 0 & -k_i & 0\end{bmatrix}\begin{bmatrix}\hat{i}_i\\ \hat{v}_c\\ \hat{i}_o\\ \hat{v}_o\\ \hat{i}_{int}\end{bmatrix} \quad (29)$$

where the symbol ^ represents the small signal value. The coefficients of the Jacobian matrix can be found in the Appendix.

Table 2 Values of the Control Gains and Parameters

Symbol	Quantity	Value
k_p	Proportional gain	0.2 A/V
k_i	Integral gain	200 A/(Vs)
k_o	Feed-forward gain	2.9
V_{ref}	Reference output voltage	35 V

5.3. Stability Analysis

Design conditions for the control parameters are derived in this subsection by applying the Routh-Hurwitz criteria to the poles of the closed-loop small-signal model. To this end, the characteristic polynomial is deduced from the Jacobian matrix expressed in (29). Following this procedure, (30) and (31) are obtained:

$$0 < k_p < k_{p.max} \quad (30)$$

$$0 < k_i < k_{i.max} \quad (31)$$

$$k_{p.max} = \frac{V_{ref}V_i(L_o + C_{eq}R^2) + C_o R^2 V_i(V_{ref} - k_o V_i) + L_i}{L_i R V_{ref}^2} \quad (32)$$

$$k_{i.max} = \frac{k_p R V_i^2 - k_o V_i^2 + 2V_{ref}V_i}{L_i V_{ref}^2} \quad (33)$$

Table 2 lists the values of the PI gains used in this study. These gains meet the above stability conditions. The values of the feed-forward gain and the reference output voltage are also included in this table. The final step in control design is to derive the control law which is represented in Fig. 3 as a comparator. This can be done taking into account the reaching condition [24]:

$$S.\frac{dS}{dt} = 0 \quad (34)$$

Therefore, the control law is obtained as:

$$u = \begin{cases}1. & S < 0\\ 0. & S > 0\end{cases} \quad (35)$$

6. Simulation and Experimental results

In this Section, the theoretical analysis of the proposed control scheme is verified by simulation and experimental results. The values of power and control parameters used in

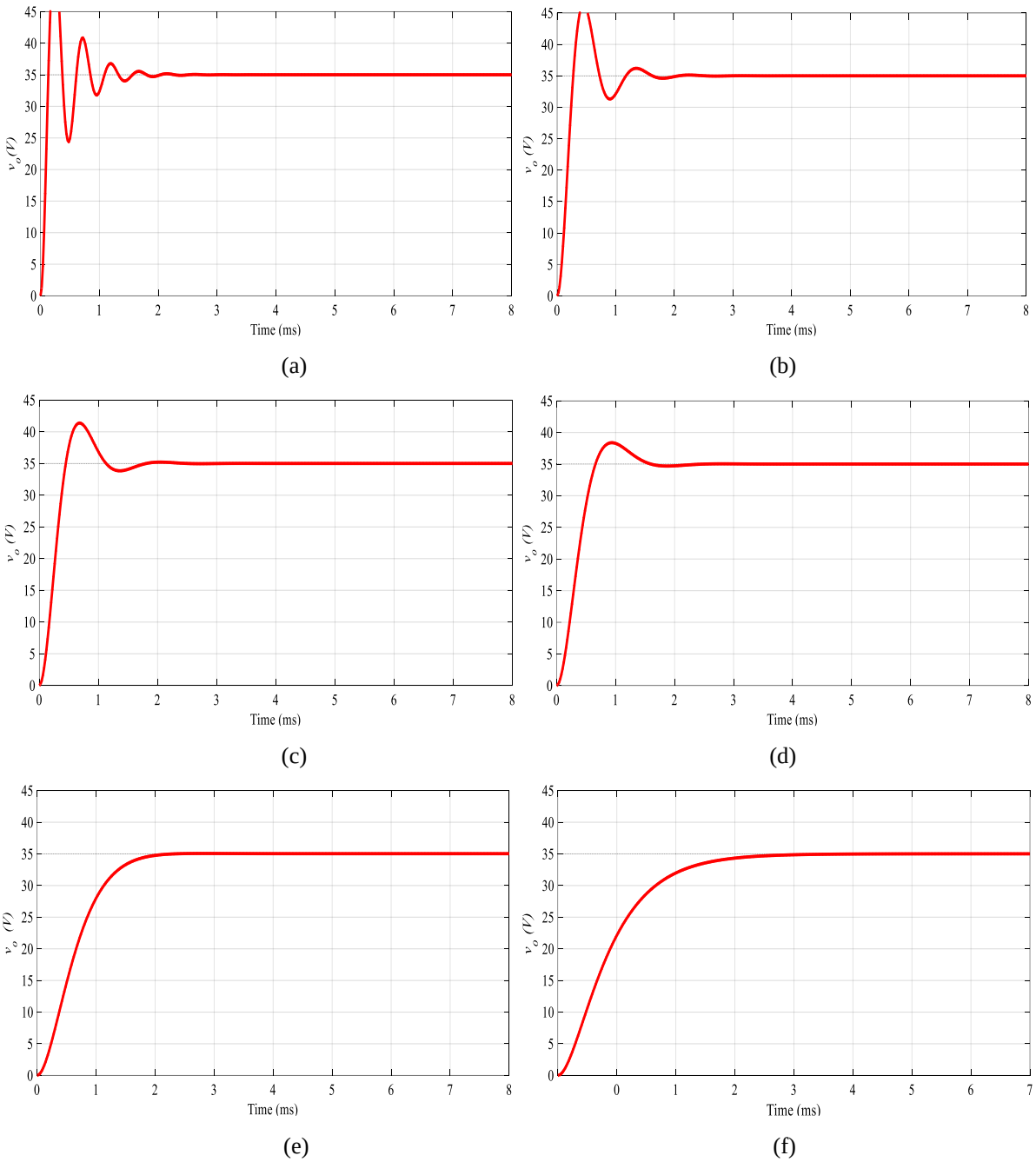

Fig. 7. *Simulation results of the output-voltage startup for the different values of* k_i *: (a) 2500, (b) 1400, (c) 700, (d) 400, (e) 200, (f) 90.*

simulation and experimental platforms are listed in Table 1 and 2.

6.1. Validation of Control Design in Start-Up Condition

Fig. 7 shows some simulation results of the closed-loop CSPRC during the output-voltage start-up for different values of k_i. Notice that a varied range of transient responses is obtained changing the gain of only this sliding surface parameter. In addition, the nominal value selected in the design (k_i = 200) provides a fast transient response without voltage overshoot.

6.2. Laboratory Prototype

A low-power laboratory prototype was constructed in a dual layer PCB design, as shown in Fig. 8. This prototype is composed of a DC-DC Class-D CSPRC as the power converter and a dsPIC33FJ16GS504-I/PT microcontroller as digital control platform. The power rating of this prototype is 60 W. The components used in the prototype are listed in Table 3.

The operation based on amplitude modulation is experimentally verified as shown in Fig. 9 for a non-periodic sequence of energising (u_k=1) and de-energising (u_k=0) modes. Notice that the peak values of the capacitor voltage are increased in energising mode and decreased in de-

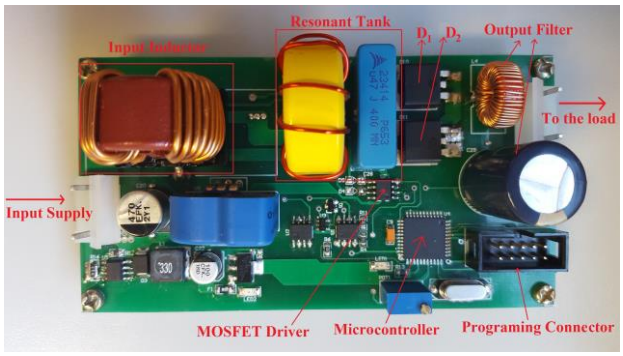

a

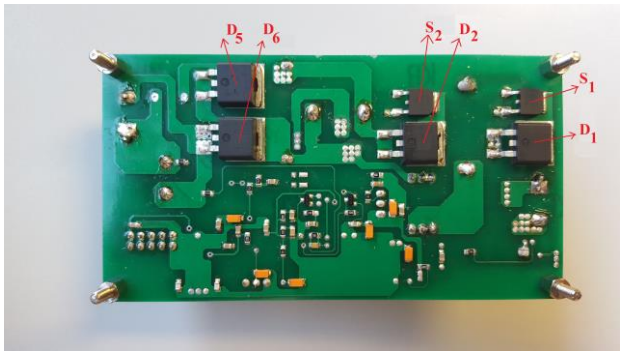

b

Fig. 8. *Experimental setup of the DC-DC CSPRC prototype*
a Top layer
b Bottom layer

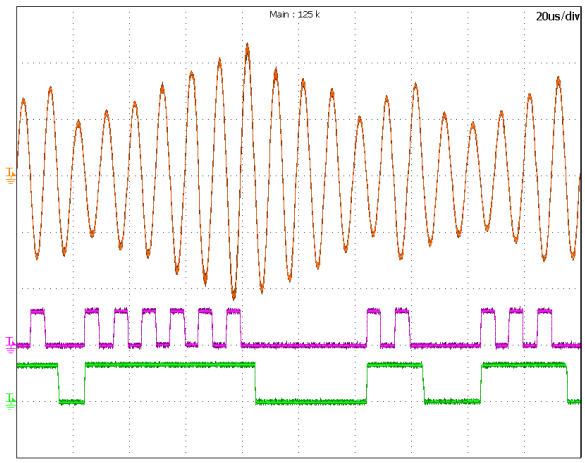

Fig. 9. *Experimental results of resonant capacitor voltage (top, 50 V/div), switching signal S_2 (middle, 20 V/div), and control signal u_k (t) (bottom, 5 V/div). Time: 20 us/div.*

energising mode. Fig. 9 also shows the driving signal for switch S_2 (see middle waveform).

6.3. Performance Evaluation in Transient State

The transient responses of the output voltage during a sudden load step change from 20 Ω to 200 Ω is shown in Fig. 10. To verify the impact of each control parameter, four different situations are considered. In the first case, the nominal control parameters are applied to the system, resulting in excellent transient and steady-state characteristics; see Fig. 10(a). In fact, the voltage deviation and settling time

Table 3 Practical Components of the Experimental Prototype

Component	Model
Diodes	20ETF08S
MOSFETs	IRFR4620
Resonant Capacitor	MKT type
MOSFET Driver	MCP14E10
Op-amps	MCP6022
Current transducers	LTP-15NP

in this case are just 2V and 0.4 ms, respectively. Some sliding surface terms are then eliminated in the next cases. For example, in second case, the feed-forward term is not considered, increasing both voltage deviation and settling time to about 6 V and 2 ms, respectively; see Fig. 10(b). This case is operationally similar to that of the closed-loop system presented in [23]. Thus, this result verifies experimentally the superior transient performance of the proposal in comparison to the dynamics obtained using the control in [23].

Note that the superiority of the first case is the consequence of the transient response improvement in finding the sliding surface. It means that in the case of load-step changes, the feed-forward term helps the modulator to rapidly find an appropriate sliding surface and consequently an adequate control signal *u* to ensure a fixed-output voltage.

In the third case, as illustrated in Fig. 10(c), the proportional gain is also eliminated, resulting in an oscillating transient response, especially during the transient between full-load to 10% of full-load. Furthermore, by eliminating the integral term, although fast transient response is obtained, the output voltage regulation is totally missed; see Fig. 10(d). Note that the largest steady-state deviations (7 V) is observed at full-load condition. These results prove that to have a fast and accurate transient response, all the sliding surface terms are essential.

Next test is to check the system robustness against resonant inductor variations. This element may experience variations of 20 % due to aging, temperature, and component tolerance. In this test however, an oversized 150 % variation in the resonant inductor is considered to enlarge the impact of this variation and facilitate the measuring of the deviations. Fig. 11 shows the transient response of the output voltage during load step changes for a resonant inductor of 13.3 uH (according to Table 1, the nominal value is 5.3 uH). Comparing these results to Fig. 10(a), it is noticed only small deviations in transient response. In this case, the voltage deviation and settling time are 1V and 0.2ms, respectively.

Fig. 12 shows the transient responses of the output voltage and input current during a voltage reference step change from 25 V to 35 V in full-load condition.

All these results prove the robustness of the proposed sliding-mode controller against the load step changes, power component variations and changes in output voltage reference.

6.4. Performance Evaluation in Steady-State

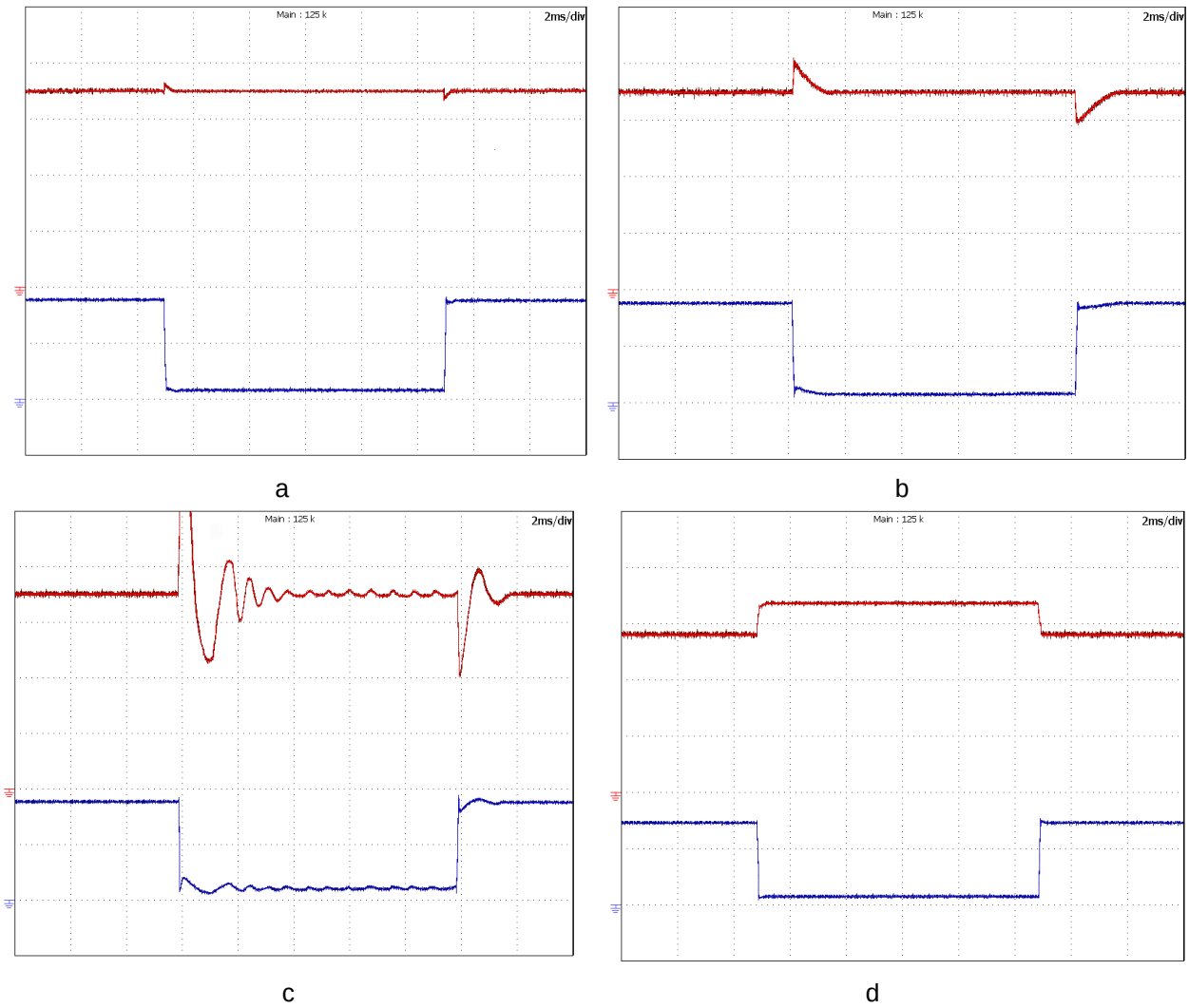

Fig. 10. *Experimental transient response to load step changes. Top: output voltage (10 V/div). Bottom: load current (1A/div)*
a Nominal control parameters shown in Table 2.
b Nominal control parameters, except $k_o = 0$
c Nominal control parameters, except $k_o = 0$ and $k_p = 0$
d Nominal control parameters, except $k_o = 0$ and $k_i = 0$

In this subsection, the performance of the converter in steady-state is evaluated. As a consequence of changes in the resonant inductor, the resonant frequency is varied. Therefore, to reproduce the operation presented in section 2, the switching frequency of the resonant converter must track the resonant frequency in real-time.

Note that, the control configuration presented in [23] suffers from high sensitivity to parameter variations. Hence, a critical efficiency analysis has been done to prove the effectiveness of the proposed control system. The comparison reveals the impact of L_r on the total efficiency of the system.

As obvious, by changing L_r, the resonant frequency is changed. Therefore, as shown in Fig. 13, once the resonant frequency differs from that of adjusted for the synchronization clock in [23], the efficiency suddenly dropped. Furthermore, for L_r values outside the plotted range, the control system in [23] becomes unstable. While for the proposed control configuration, the efficiency is kept constant for different values of L_r. The reason is that in this case, the switching frequency of the resonant converter is always pursuing the resonant frequency as a consequence of the synchronization process explained in Section 4.

Fig. 14 shows the steady-state waveforms of the resonant capacitor voltage for a resonant inductor value of 5.3 µH (nominal value). In this case, the resonant frequency is about 100 kHz. The control signal u(t) is perfectly synchronized with the resonant capacitor voltage.

Fig. 15 shows again the steady-state waveform of the resonant capacitor voltage but now for a resonant inductor of 13.3 µH. In this case, the measured switching frequency is around 82 kHz which is successfully tracked by the proposed controller (see Fig. 6), proving the robustness of the modulator to track the resonant frequency for different values of the resonant inductor.

Fig. 16 shows the steady-state voltage across the right and left leg of the class-D inverter shown in Fig. 1 and their associated current. This figure also reveals the ZVS operation of the CSPRC. Note that the voltage of S1 is positive in OFF state while in S2 is positive and negative, according to the principle of operation illustrated in Fig. 2 and 3. In S2, both

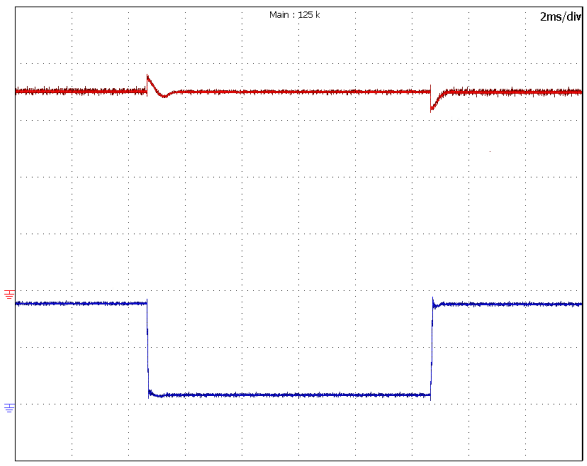

Fig. 11. *Experimental load transient response for L_r = 13.3 μH. Up: Output voltage (10 V/div). Bottom: output current (1 A/div)*

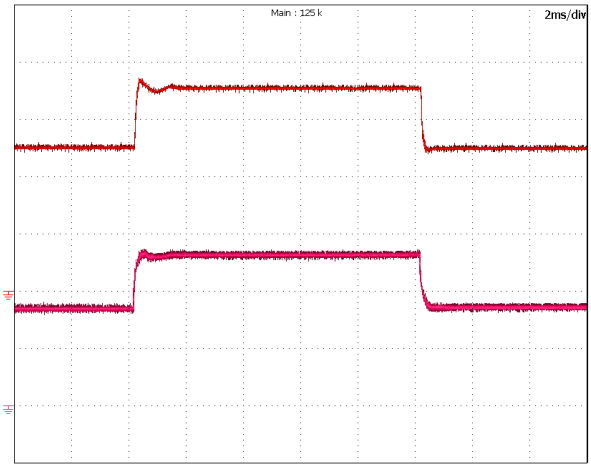

Fig. 12. *Experimental transient response to voltage reference step changes. Top: output voltage (10 V/div). Bottom: input current (2A/div)*

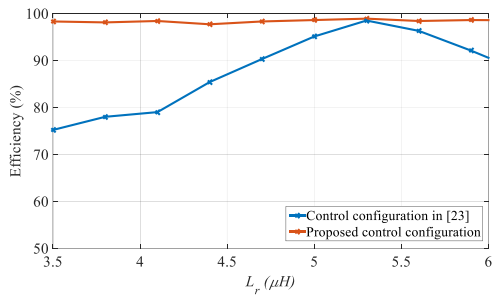

Fig. 13. *The impact of L_r on the total efficiency of the converter*

voltage polarities are possible due to the diode D2 in series with S2.

7. Conclusion

Voltage-source series resonant converters are extensively used in applications requiring resonant technology. Although current-source parallel-resonant converters show promising features, these configurations are

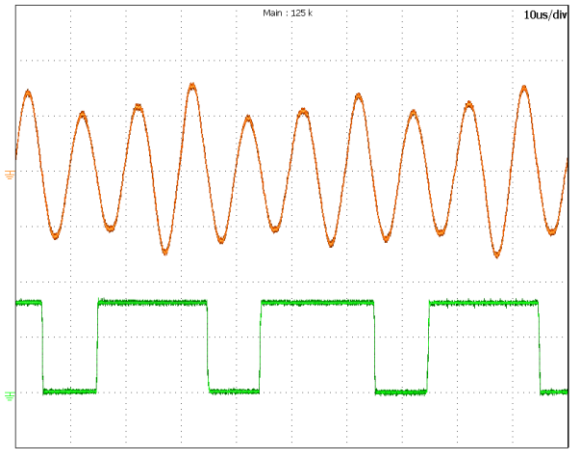

Fig. 14. *Steady-state waveforms for L_r=5.3 μH Up: Resonant capacitor voltage (50 V/div). Bottom: control signal $u_k(t)$ (2 V/div)*

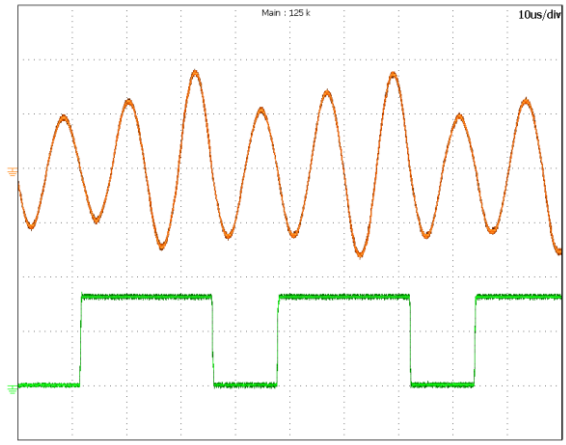

Fig. 15. *Steady-state waveforms for L_r=13.3 μH. Up: Resonant capacitor voltage (50 V/div). Bottom: control signal $u_k(t)$ (2 V/div)*

used less in practice, probably because of their greater complexity.

With the aim to extend the application of CSPRC, in this paper, a sliding-mode control has been proposed for the class-D CSPRC converter operating with amplitude modulation. The combination of the proposed controller and modulator leads to a robust system against load changes and power component variations. As demonstrated experimentally, the switching frequency adapts automatically to changes in resonant component values while maintaining zero voltage switching conditions. Regardless of the impact of the PI terms to regulate the output voltage, the feed-forward term plays a significant role to obtain a fast transient response during load step changes. The proposed control scheme constitutes the first contribution of this paper.

A theoretical study conducting to the design of the closed-loop controller is also proposed in the paper. The procedure starts with the derivation of the closed-loop dynamic model. Next, a stability analysis is performed to obtain the valid range for the control parameters. This theoretical study constitutes the second contribution of the paper.

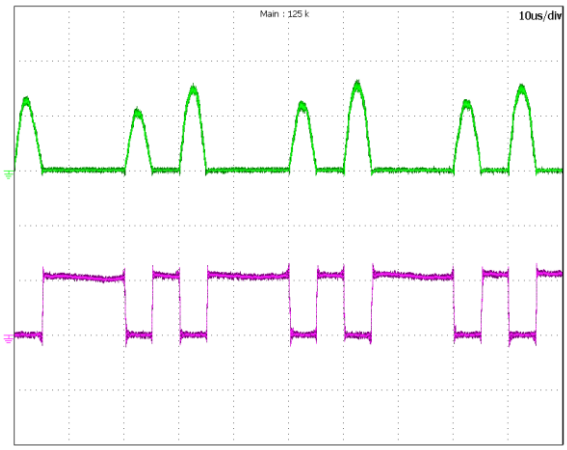

a

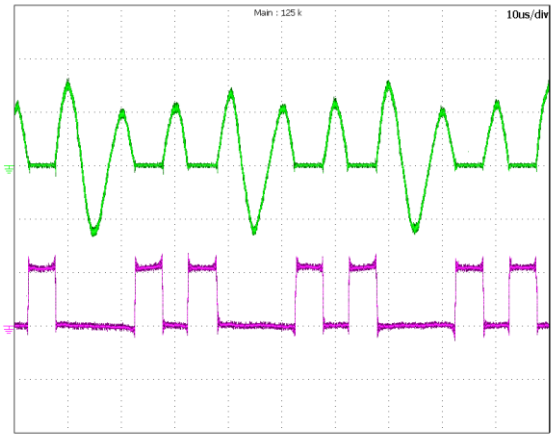

b

Fig. 16. *Steady-state switch voltage (green, 50 V/div, 10 µs/div) and current (pink, 5 A/div).*
a Switch S1
b Switch S2

The proposed controller can be applied to other current-source resonant topologies including half-bridge, full-bridge and other configurations by slightly modifying the logic circuit of the modulator. This is a promising approach to be employed in applications such as inductive contactless-energy transfer systems, plug-in vehicle charging, charging mobile electrical devices, charging medical device implants, etc. Future research is directed to this subject in order to adapt the proposed robust and fast control scheme to be a successful solution for these applications.

8. Appendix

This Appendix shows the coefficients of the Jacobian matrix expressed in (29):

$$J_{12} = \frac{k_o}{L_o} \tag{A1}$$

$$J_{13} = \frac{-k_p}{C_o} \tag{A2}$$

$$J_{14} = -k_i - \frac{k_o}{L_o} + \frac{k_p}{\mathrm{R}C_o} \tag{A3}$$

$$J_{21} = \frac{V_i}{C_{eq}V_{ref}} \tag{A4}$$

$$J_{22} = -\frac{(L_oV_i + L_ik_oV_{ref})}{L_oRV_iC_{eq}} \tag{A5}$$

$$J_{23} = \frac{(L_ik_pV_{ref} - C_oRV_i)}{C_oRV_iC_{eq}} \tag{A6}$$

$$J_{24} = \frac{L_iV_{ref}(k_i + \frac{k_o}{L_o} - \frac{k_p}{C_oR})}{RV_iC_{eq}} \tag{A7}$$

9. Acknowledgments

This work has been supported by ELAC2014/ESE0034 from the European Union and its linked Spanish national project PCIN-2015-001. We also appreciate the support from the Ministry of Economy and Competitiveness of Spain and the European Regional Development Fund (FEDER) under project ENE2015-64087-C2-1-R.

10. References

[1] Thenathayalan, D., Lee, C. g. and Park, J. H.: 'High-order resonant converter topology with extremely low-coupling contactless transformers', *IEEE Trans. Power Electron.*, 2016, **31**, (3), pp. 2347-2361

[2] Tan, X., and Ruan, X.: 'Equivalence relations of resonant tanks: a new perspective for selection and design of resonant converters', *IEEE Trans. Ind. Electron.*, 2016, **63**, (4), pp. 2111-2123

[3] Lee, S. H., Cho, Y. W., Cha, W. J., *et al.*: 'High efficient series resonant converter using direct power conversion', *IET Power Electronics*, 2014, **7**, (12), pp. 3045-3051

[4] Zhang, X., Green, T. C., and Junyent-Ferré, A.: 'A new resonant modular multilevel step-down DC–DC converter with inherent-balancing', *IEEE Trans. Power Electron.*, 2015, **30**, (1), pp. 78-88

[5] Lu, J., Perreault, D. J., Otten, D. M., and Afridi, K. K.: 'Impedance control network resonant DC–DC converter for wide-range high-efficiency operation', *IEEE Trans. Power Electron.*, 2016, **31**, (7), pp. 5040-5056

[6] Lin, B. R., and Cheng, P. J.: 'New ZVS DC-DC converter with series-connected transformers to balance the output currents', *IEEE Trans. Power Electron.*, 2014, **29**, (1), pp. 246-255

[7] Tang, Y., and Khaligh, A.: 'Bidirectional resonant DC–DC step-up converters for driving high-voltage actuators in mobile microrobots', *IEEE Trans. Power Electron.*, 2016, **31**, (1), pp.340-352

[8] Lee, I. O.: 'Hybrid DC–DC converter with phase-shift or frequency modulation for NEV battery charger', *IEEE Trans. Ind. Electron.*, **63**, (2), pp. 884-893

[9] Soeiro, T. B., Mühlethaler, J., Linnér, J., P., and Kolar, J. W.: 'Automated design of a high-power high-frequency

LCC resonant converter for electrostatic precipitators', *IEEE Trans. Ind. Electron.*, **60**, (11), pp. 4805-4819

[10] Martín-Ramos, J. A., Vaquero, Ó.P., Villegas, P. J., Martínez, J. A., and Pernía, A. M.: 'Multilevel PRC-LCC resonant converter for X-ray generation, ' *Electronics Letters*, 51, **15**, pp. 1189-1191

[11] Zhao, B., Yu, Q., and Sun, W.,: 'Extended-phase-shift control of isolated bidirectional DC–DC converter for power distribution in microgrid', *IEEE Trans. Power Electron.*, 2012, **27**, (11), pp. 4667-4680

[12] Chen, F. Y., Liang, T.J., Lin, R. L., and Chen, J. F.: 'A novel self-oscillating, boost-derived DC-DC converter with load regulation', *IEEE Trans. Power Electron.*, 2005, **20**, (1), pp. 65-74

[13] Iqbal, S., Singh, G. K., and Besar, R.,: 'A dual-mode input voltage modulation control scheme for voltage multiplier based X-ray power supply', *IEEE Trans. Power Electron.*, **23**, (2), pp. 1003-1008

[14] Castilla, M., Garcia de Vicuña, L., Matas, J., Miret, J., and Vasquez, J. C.: 'A comparative study of sliding mode control schemes for quantum series resonant inverters', *IEEE Trans. Ind. Electron*., 2009, **56**, (9), pp. 3487–3495

[15] Sosa, J., Castilla, Miret, M., Garcia de Vicuna, L., and Moreno, L. S.: 'Sliding-mode input-output linearization controller for the DC/DC ZVS CLL-T resonant converter', *IEEE Trans. Ind. Electron*., 2012, **59**, (3), pp. 1554–1564

[16] Sosa, J., Castilla, Miret, M., Garcia de Vicuna, L., and Matas, J.: 'Modeling and performance analysis of the DC/DC series-parallel resonant converter operating with discrete self-sustained phase-shift modulation technique', *IEEE Trans. Ind. Electron*., 2009, **56**, (3), pp. 697–705

[17] Hu, A. P., Covic, G. A., and Boys, J. T.: 'Direct ZVS start-up of a current fed resonant inverter', *IEEE Trans. Power Electron.*, 2006, **21**, (3), pp. 809–812

[18] Namadmalan, A., and Moghani, J. S.: 'Self-oscillating switching technique for current source parallel resonant induction heating systems', *J. Power Electron.*, 2012, **12**, (6), pp. 851–858

[19] Namadmalan, A., and Moghani, J. S.: 'Tunable self-oscillating switching technique for current source induction heating systems', *IEEE Trans. Power Electron.*, 2014, **61**, (5), pp. 2556–2563

[20] Dai, X., and Sun, Y.: 'An accurate frequency tracking method based on short current detection for inductive power transfer system', *IEEE Trans. on Ind. Electron.*, 2014, **61**, (2), pp. 776-783

[21] Namadmalan, A.: 'Bidirectional current fed resonant inverter for contactless energy transfer Systems', *IEEE Trans. Ind. Electron.*, 2015, **62**, (1), pp. 238–245

[22] Sabanovic, A.: 'Variable structure systems with sliding modes in motion control—A Survey', *IEEE Transactions on Industrial Informatics*, 2011, **7**, (2), pp. 212-223

[23] Castilla, M., Garcia de Vicuña, L., Lopez, M., and Font, J.: 'A sliding mode controller for the current-source parallel-resonant converter with zero-voltage switching', *Proc. of IEEE IECON*, 1997, New Orleans, LA, pp. 477-482

[24] Haroun, R., Cid-Pastor, A., Aroudi, A. E., and Martínez-Salamero, L.: 'Synthesis of canonical elements for power processing in DC distribution systems using cascaded converters and sliding-mode control', *IEEE Trans. Power Electron.*, 2014, **29**, (3), pp. 1366-1381

[25] Slotine, J. J., and Li, W.: 'Applied Nonlinear Control', (Englewood Cliffs, NJ: Prentice-Hall, 1991)